Insights into the impact and solidification of metal droplets in ground-based investigation of droplet deposition 3D printing under microgravity

Jieguang Huang[1], Lehua Qi[1], Jun Luo[1]*, Xianghui Hou[2]*

1. School of Mechanical Engineering, Northwestern Polytechnical University, Xi'an 710072, China.

2. Faculty of Engineering, University of Nottingham, Nottingham NG7 2RD, United Kingdom

*Corresponding author: qilehua@nwpu.edu.cn (L. Qi); luojun@nwpu.edu.cn (J. Luo).

Abstract

Droplet deposition 3D printing is an additive manufacturing technique offering a great potential for metal parts fabrication in space, of which some preliminary testing is usually performed on ground in the early research. The previous work mimicked the anti-gravity deposition of molten metal droplet through manipulating it into perpendicularly depositing on a vertical substrate. However, the ground-based simulation of droplet deposition 3D printing under microgravity remains an elusive goal, since the spreading and receding processes are still affected by gravity. To address this issue, the prevailing physical mechanisms of gravity effect on droplet impact and solidification are urgent to be defined. Here, we present the studies on the impact dynamics and transient solidification of the molten metal droplet deposited on vertical substrates through numerical modeling and experiments. It is observed that the spreading and retraction of the droplet are asymmetric, besides its solidification shape tilts to gravitational direction. The formation mechanisms of these undesired behaviors are further demonstrated. The results show that the asymmetrical spreading, retraction and solidification shape of the droplet originate from the interaction of gravity and solidification. Moreover, the tilt of the solidified droplet has a correlation with the critical process parameters, i.e. impact velocity, temperatures of droplet and substrate. With a larger impact inertia and a lower solidification rate, the undesired solidification shape can be effectively eliminated. This work provides a foundation for the further investigation of the ground-based physical simulation of outer space droplet deposition 3D printing.

Keywords: 3D printing; metal droplet; solidification; vertical substrate; gravity effect.

1. Introduction

Replacing worn or damaged parts in spacecraft during deep-space exploration or asteroids and Mars visiting is inevitable. However, it is time consuming and costly to transport resupplies as the space is isolated [2–5]. To this end, Additive Manufacturing (AM) is introduced to space manufacturing [6–9] for the advantages of low cost, wide material applicability, high precision, and low-unit on-demand. The droplet-based 3D printing technology [10,11] is believed to be a promising technique for advance in-space manufacturing without using large energy equipment or custom materials [12].

Depositing droplets on a vertical substrate perpendicularly is assumed to be a viable method to preliminarily demonstrate the feasibility of droplet deposition 3D printing in microgravity. Because the droplets do not respond to gravity in the direction of deposition, owing to the inertia resulting from impact velocity is separated from the gravity [13,14]. Huang et al. [1] mimicked the anti-gravity deposition of droplets in normal gravity environment by using electric field to manipulate the droplets to perpendicularly deposit on a vertical substrate. However, the droplet is no more subject to electric field force (a balance force of gravity) due to charge transfer at the moment of landing on the substrate. Consequently, the spreading and receding processes will be affected by gravity, resulting in irregular solidification shape of the deposited droplet. That is undesired for the ground-based simulation of droplet deposition 3D printing under microgravity. It is prerequisite to unveil the gravity effects for the proposal of elimination strategies. To this end, the impact dynamics and solidification of droplets impacting onto vertical substrates should be investigated.

When a droplet retains on vertical substrates, it is subject to capillary force, viscous force, surface tension, solidification drag, and gravitational force which is a source term that makes the impact dynamics differ from the deposition of droplets on a horizontal solid wall. Considerable works have been reported regarding the effects of gravitational force on the form of sessile droplets. Podgorski et al. [15] identified the dependence of the capillary number (from here on *Ca*, which is the ratio of viscous force to surface tension, $Ca = \mu v_0 / \sigma$) on tangential Bond number (from here on Bo_c, which is the ratio of tangential gravity to surface tension, $Bo_c = \rho g_c {d_0}^2 / \sigma$), which governs different states of a droplet staying on or running down along an inclinational substrate. Droplets with small *Ca* (smaller than the capillary length) and Bo_c numbers show shapes of circles or ovals. By investigating the contact line shapes of sessile water droplets with different scales on inclination surface, Annapragada et al. [16] found that the droplet contact area was almost circular due to the low Bo_c number. Milinazzo et al. [17] numerically studied the shape of a droplet on a vertical wall. Their results show that the wetted area keeps unchanged on condition that *Bo* number is smaller than a critical value, which is dependent on the static contact angle.

In contrast to sessile droplet attached on an inclinational substrate, when a droplet that ejected along free-fall direction impacts on the inclinational substrate, it will be subject to an extra inertia force induced by impact velocity. The droplet spreads, retracts, oscillates, or may even roll and slide on the substrate [18,19]. The dynamic behaviors vary with the inclination angle since the impact velocity of the droplet is not perpendicular to the substrate surface [17,18]. That brings a tangential velocity component which is parallel to the substrate surface. The tangential velocity associated with the inclination angle of the substrate has a significant effect on the droplet impact dynamics [22]. Accordingly, the dynamic behaviors of droplets perpendicularly impacting on vertical substrates would be of difference since the tangential velocity component is 0. Moreover, the difference will be intensified by metal droplet as solidification drag is introduced in the surface flow. Unfortunately, there are limited literatures that reported the impact mechanism of metal droplets on a vertical substrate.

The aim of this work is to provide insights into the impact and solidification of metal droplets on vertical substrates. A molten metal droplet horizontal ejection and deposition experimental system is used to eject metal micro-droplets horizontally. As the droplet impacts on vertical substrates, the dynamic behaviors are snapshotted by a high speed camera. The evolutions of spreading factor, vertex height and solidification contour of the dynamic droplet are investigated. Based on these investigations, the gravity effects on impact and solidification are analyzed. Finally, the dependences of the solidification shape of the deposited droplet on the *Fr* number ($Fr = {v_0}^2 / d_0 g$), *SHP* number ($SHP = (T_d - T_m)/(T_d - T_{sub})$), and *Ste* number ($Ste = C_l (T_m - T_{sub})/L$) of the droplet are studied. The definition of these dimensionless numbers are from the critical processing parameters[23]: impact velocity, temperatures of droplet and substrate, which are given in Equation (2)-(3).

2. Research methods

2.1. Experimental approach

The schematic of the deposition system is shown in Fig. 1 (a). It mainly includes a micro droplets horizontal generator, a 3D platform, a low oxygen environment maintenance system (glove box filled with Argon), and a high speed camera with an acquisition rate of 100 kfps (i-SPEED 720, England). The system works as follows: first, raw Sn-63 wt% Pb was melted in a graphite crucible; then, started the generator; under the periodic actuation of the vibration bar, molten metal droplets were ejected on demand. The vibration bar was driven by piezoceramics. The ejection frequency was 1 Hz, the orifice diameter was ~200 μm. The substrate was shifted by the 3D platform, and heated through the substrate heater. The substrate material was copper sheet (50 mm × 30 mm × 2 mm), which was mechanically polished before the experiment with the same roughness (see Table 1) to make sure an consistent initial contact condition. The dynamic processes of droplet impacting under three different initial conditions (as listed in Table 1) were snapshotted by the high speed camera.

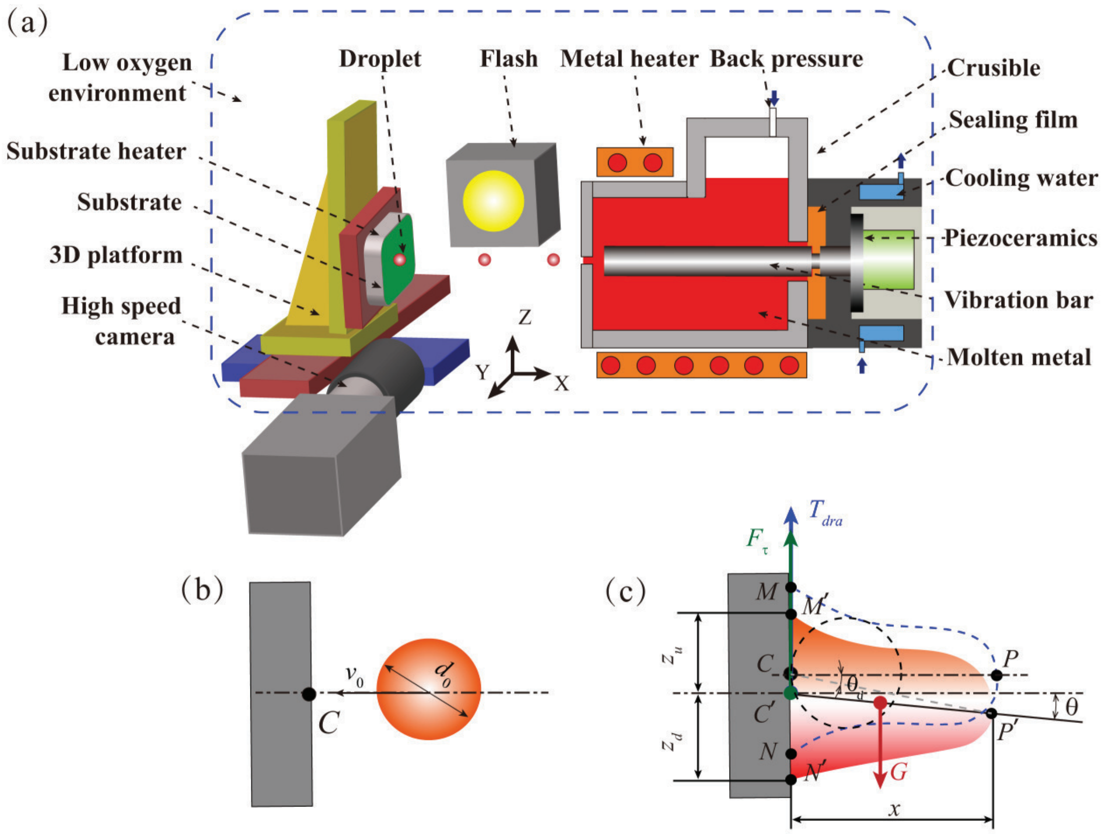

Fig. 1. Schematics of (a) experimental system, (b) droplet being about to impact, and (c) droplet receding.

Fig. 1 (b) and (c) are transient schematics of droplet being about to impact and receding on a vertical substrate, respectively. C is the contact point, while C' is the central point of the contact area of the solidified droplet. M (M') and N (N') denote the upper and lower rim of the deposited droplet, respectively. Assuming microgravity environment, the ideal contour of the receding droplet is $CMPNC$. In contrast, the droplet recedes with a contour of $C'M'P'N'C'$ under gravity. The contour is no more symmetric. Herein, a parameter tilt angle θ is defined to characterize the asymmetry of the solidified droplet induced by gravity effects. θ is the angle between the bisector $C'P'$ of the droplet cross-section area and the normal line CP of the vertical substrate surface. The dynamic variation of the tilt angle is characterized as θ_d. Moreover, z and x are introduced to characterize the spread radius and the height of the droplet vertex (denoted by P'), respectively. z_u and z_d are the length of $C'M'$ and $C'N'$, respectively. The subscripts *u* and *d* respectively represent the upward and downward rims of the droplet. The values of θ, *z* and *x* were calculated from the snapshots of the dynamic contours in droplet impacting via a home-made image processing algorithm programed with Matlab R2015a. The main function of the algorithm is to get the coordinate of the key points *C*, C', M', N', P' at first, and then to calculate the geometric relationships.

Table 1
Parameters in experiments and simulation.

Case	T_d (°C)	T_{sub} (°C)	Ra (μm)	Substrate Material	v_0 (m/s)	d_0 (μm)	*We*	*Ste/Pr*
Case 1	250	50	0.23	Cu	1.70	273.7	13.5	10.8
Case 2	250	170	0.23	Cu	1.66	279.3	13.1	4.3
Case 3	250	240	0.23	Cu	1.61	279.8	12.3	0.5

In order to ensure the droplet perpendicularly impact on the substrate, proper deposition distance is crucial because the velocity increment during droplet flight could be neglected in such distance. Fig. 2 shows the dependence of the solidification shape of droplets on the deposition distance with an initial velocity of ~1 m/s, an initial droplet temperature of ~250 °C, and an initial substrate temperature of ~140 °C. The tilt angle of the solidified droplet is constantly equal to ~1° when the deposition distance is less than 5 mm, suggesting that the solidification shape is independent of gravity under certain condition. In our experiment, the distance between the nozzle and the substrate was ~3.5 mm. The velocity in the gravitational direction is at a ratio of ~3.5% to the ejection velocity (~1 m/s). Therefore, the droplet is presumed to perpendicularly impact on the substrate.

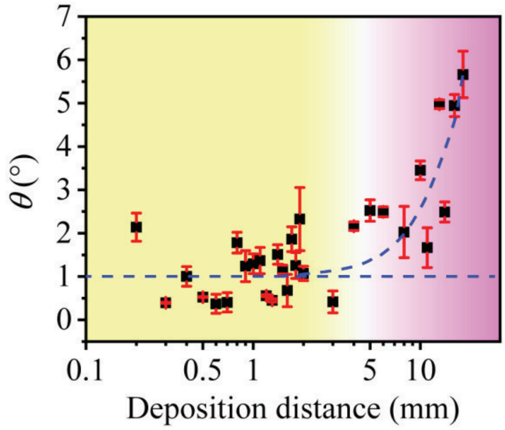

Fig. 2. Dependence of the solidification shape on deposition distance.

2.2. Numerical approach

In order to investigate the flow field during droplet impacting, spreading, oscillating, and solidifying on vertical substrates, a numerical model was established using the volume of fluid (VOF) method [24–26]. The mathematical principle of this simulation model is similar to our previous work [27,28]. The computation domain of the numerical model is shown in Fig. 3. The shape of the droplet was assumed to be a sphere, even though the droplet was slightly oscillating during flight. The initial impact velocity of the droplet was regarded as uniform. The fluid field was assumed as incompressible laminar flow, for the Reynolds number of the metal melt is less than 2300. The incompressible N-S (Navier-Stokes) and continuity equations were used to govern the fluid dynamic processes of the droplet. The enthalpy conservation equation was used to solve the temperature field of the droplet. Since heat transfer to the environment was far less than that to the substrate, the heat dissipation of the droplet was ignored [28].

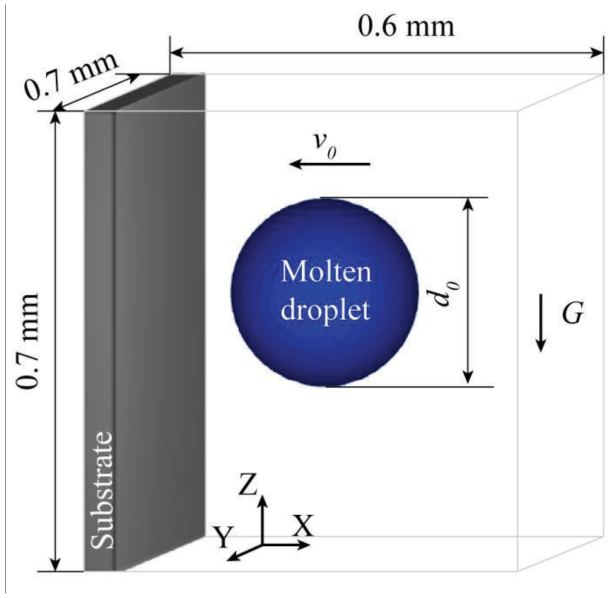

Fig. 3. Computation domain of the numerical model.

Since the computation domain is tiny (0.7 mm × 0.7 mm × 0.6 mm in size), the convection between the ambient environment and the droplet could be ignored. The boundary conditions were all set as "continuative" except for the substrate surface. For the thickness of substrate (2 mm in size, and made of copper with a high thermal conductivity of 386 W/m·K) was about 10 times larger than the droplet diameter, the isothermal "wall" boundary condition was applied to substrate surface. Then, it is noteworthy to note that there is a heat transfer when the molten droplet contacts with the substrate. The heat exchange efficiency is characterized by heat transfer coefficient h_c. h_c is very sensitive to the thermal contact conditions, which are dependent of surface roughness. The coefficient is commonly selected through repeated experimental observations [29–32]. Accordingly, this parameter was set as 6.7×10^5 W/m^2·K in the present simulation. For the same reason, the contact angle was set as 150°. The thermo-physical properties of the Sn-63 wt% Pb are listed in Table 2. The subscripts l and s represent the property for liquid phase and solid phase at the temperature of 250

°C and 20°C, respectively.

A commercial software FlOW-3D 11.2.2.01 was used to implement the numerical model developed above. All initial parameters of droplet, such as the surface tension, contact angle, dimension, velocity, position and temperature can be set in a droplet generating subroutine provided by FlOW-3D. The finite volume method was employed to solve the Navier–Stokes equations for fluid field. Equations were iteratively solved by using a minimum time step of 10^{-9} s. The computational grid consisted of about 440,000 rectangular elements, equaling about 30 units per droplet diameter.

Table 2
Thermo-physical properties of Sn-63 wt% Pb.

Properties	Value
Density (kg/m^3)	$\rho = 8400$
Dynamic viscosity (Pa·s)	$\mu = 0.0013$
Surface tension coefficient (N/m)	$\sigma = 0.494$
Latent heat for solidification (J/kg)	$L = 37000$
Heat conductivity coefficient (W/m·K)	$k_l = 26$
	$k_s = 50.9$
Specific heat capacity (J/kg·K)	$C_l = 203$
	$C_s = 167$
Liquidus temperature (°C)	$T_{liquid} = 183$
Solidus temperature (°C)	$T_{solid} = 183$
Contact angle (°)	$\theta_a = 150$

2.3. Numerical model validation

The simulation results of droplet impacting on vertical substrate are shown in Fig. 4. The initial condition coincides with Case 1 in Table 1. Fig. 4 (a) shows the simulation snapshots of droplet impacting on a vertical substrate. In comparison with the experimental phenomena of Case 1 in Fig. 5, the development of the droplet shapes versus time shows good agreement. Furthermore, the comparison of numerical spreading factors to the experimental results of Case 1 is presented in Fig. 4 (b). They also agree well with each other, which proved the accuracy and feasibility of the numerical model.

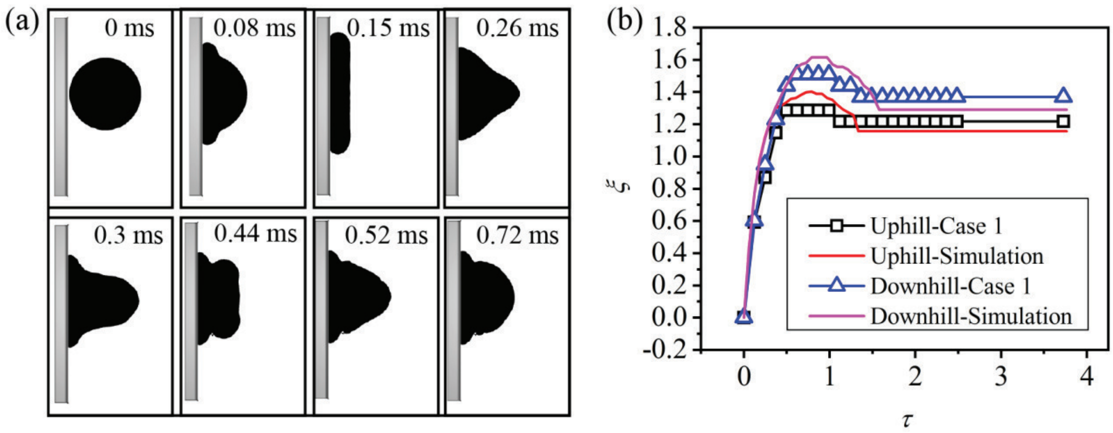

Fig. 4. Simulation results of droplet impingement (a) snapshots, (b) comparisons to experimental spreading factors.

3. Results and discussions

To analyze the droplet impact dynamic and thermal behaviors, dimensionless parameters including normalized time (τ), spread factor (ξ), dimensionless bump height (γ), Stefan number (*Ste*) , superheat parameter (*SHP*) [33], Bond number (*Bo*), Froude number (*Fr*), and Weber number (*We*) are defined as follows.

$$\tau = \frac{tv_0}{d_0}, \quad \xi = \frac{z}{d_0}, \quad \gamma = \frac{x}{d_0} \tag{1}$$

where t, v_0, d_0, z, x are time, initial velocity of droplet, droplet diameter, spread radius, height of droplet vertex, respectively.

$$Ste = \frac{C_l(T_m - T_{sub})}{L}, \qquad SHP = \frac{T_d - T_m}{T_d - T_{sub}} \tag{2}$$

where T_m is droplet melting point, T_{sub}, and T_d are initial temperature of substrate and droplet.

$$Fr = \frac{v_0^{\ 2}}{d_0 g}, \ We = \frac{\rho d_0 v_0^2}{\sigma}, \ Bo = \frac{\rho g d_0^{\ 2}}{\sigma} \tag{3}$$

where g is gravity acceleration.

3.1. Impact and solidification of a metal droplet on a vertical substrate

To unveil the gravity effects on impact and solidification, the dynamic processes of metal droplets horizontally impact on vertical substrates with different initial substrate temperatures (as listed in Table 1) were investigated. As shown in Fig. 5, the fluid dynamics processes consist of four stages: impact, spreading, receding and oscillation. When the droplet impacts on a substrate, it spreads outward immediately. After the contact line stretches to the maximum extent, the flow retracts back. The impact processes are analogous with different thermal contact conditions in Case 1- Case 3, whereas the subsequent stages and solidification shapes behave differently. In addition, the contact angles of the upper rims of the droplets are different from the lower ones during the spread and retraction processes. The differences in contact angle vary periodically and appear to be more significant with the increase of the substrate temperature. This phenomenon was not observed in the regime that droplets impact on a horizontal surface [34,35], where the dynamic droplet is axial symmetry, and thus the contact angles of the droplet rim are coincident.

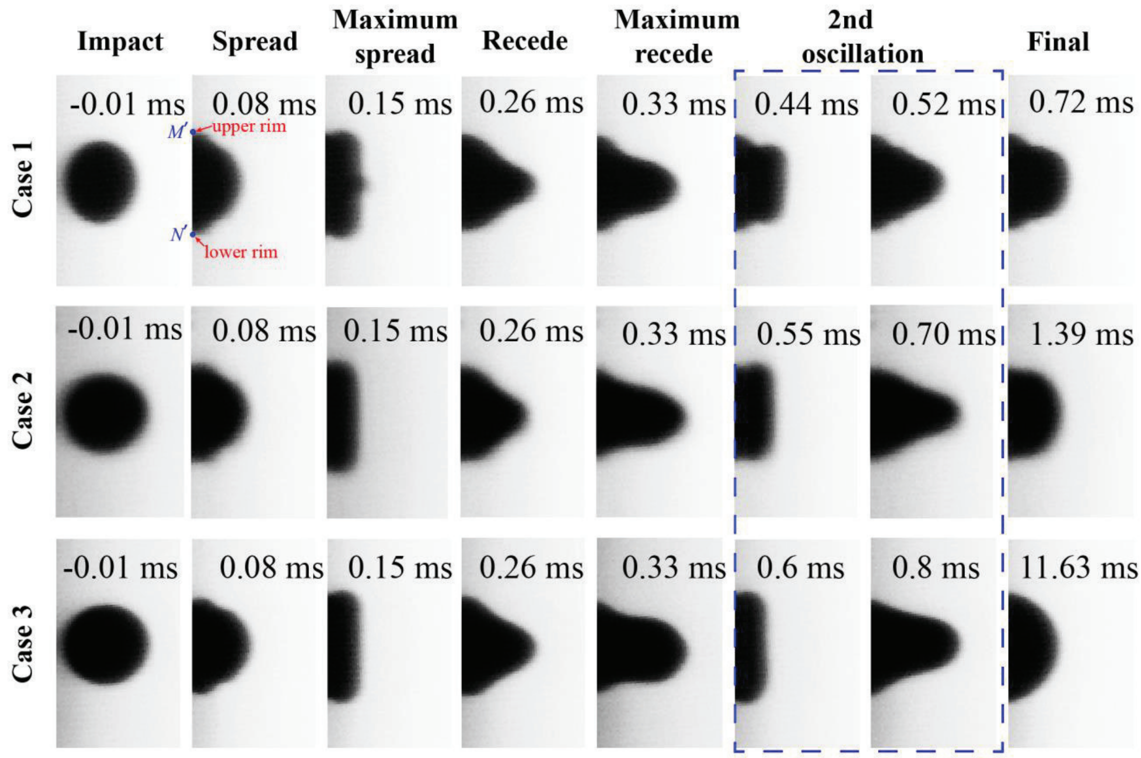

Fig. 5. Snapshots of molten metal droplets impacting on vertical substrates under different thermal contact conditions (Case 1- Case 3).

3.1.1. Mechanisms on the formation of asymmetrical spreading

It is generally known that the spreading factor is a critical parameter characterizing the droplet impact and solidification processes. To further investigate the spreading difference between the upper rim and the lower rim, the evaluation of the spread factor ξ versus dimensionless time τ is investigated. Fig. 6 (a) and (b) show the migration of the upper and lower rims of the droplet, respectively. The maximum spread factors of the upper rim in Case 1- Case 3 are all equal to 1.28, while the lower ones equal to 1.51, 1.52 and 1.58, respectively. The spread factor of the lower rim undergoes an increase with the growth of substrate temperature due to different solidification rate of the contact line of droplet. Compared to surface tension and viscous dissipation, the effect of solidification on droplet spreading can be quantified by a dimensionless parameter ϕ [31]. During the spreading processes, solidification could be neglected if

$$\phi = \frac{Ste}{\sqrt{Pr}}\sqrt{\frac{\eta_s}{\eta_d}} < 1 \qquad (4)$$

where $Pr = \mu C_l / k_l$, $\eta = k\rho C$, the subscripts s and d represent substrate and droplet repectively. For Case 1- Case 3, the values of ϕ approximately equal 6, 3.3, and 0.3, respectively. Accordingly, solidification plays an important role in resisting the spreading process in Case 1 and Case 2. The solidified melt around the edges of spreading droplet will form a solid rim that obstructs the surface flow, resulting in that the motion of the contact line ceases during receding. In contrast, in Case 3, the droplet oscillates continually owing to a higher substrate temperature than the melting point of droplet. What is of interest is that for all cases the spread factors of the upper rims are smaller than those of the lower ones, while the retraction of the upper rim is more obvious comparing to the lower ones. We supposed that the differences in the spreading and retraction of the upper and lower rims come from the effects of gravity. To validate this supposition, we investigated the gravity effects on the spreading and retraction velocity and characteristic time for spreading and receding of the impacted droplet.

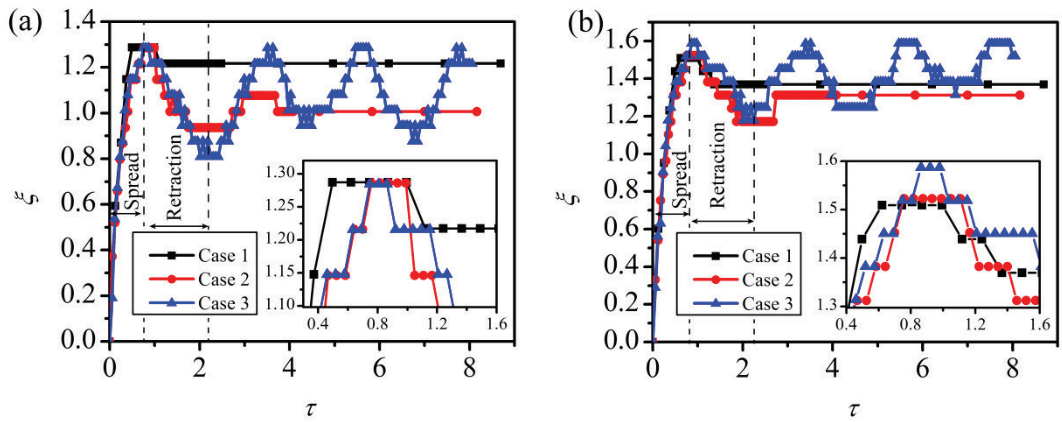

Fig. 6. Variations of the spread factor versus time for the droplet in Case 1-3: (a) uphill spread, (b) downhill spread.

To understand the gravity effects on the spreading and retraction velocity of the impacted droplet, the evolution of the fluid field of the droplet in Case 1 versus spreading time was numerically calculated. We designated five specific points on the interface (labeled as *A*, *B*, *O*, *E*, *F* as shown in Fig. 7 (a)) to monitor the velocity field. Points *A*, *B*, *O* are on the route the upper rim of the droplet spreads, and *E*, *F* are on the route the lower rim of the droplet spreads. Point *O* is a symmetrical point of *A* (*B*) and *E* (*F*). The variations of the velocity of each point versus time under different gravity levels (0 g, 1 g, 10 g, and 100 g) are shown in Fig. 7 (b). τ=0 corresponds to the instant that the droplet impact on the substrate. The negative velocity denotes the fluid flows along the gravity direction, in contrast, the positive velocity represents a reverse flowing direction. Initially, the spreading velocity is small as the velocity curve of point *O* shows. As the droplet continues to spread forward, the contact line successively pass over point *O*, *E*, *B*, *F*, *A*. The velocities at points *A* and *B* are respectively smaller than those at points *F* and *E*, suggesting that the spreading velocity of the lower rim is faster compared to the upper rim. Based on Newton's law, we can conclude that the upper rim of the droplet experiences a deceleration of gravity, but the lower rim experiences acceleration by gravity. The differences in the velocity peak (marked in Fig. 7 (b)) of each point pairs (E→B and F→A) are shown in Fig. 7 (c). With the increase of the gravity level, the velocity differences tend to be more obvious, especially at droplet retraction stage. It is noteworthy that the velocity of Point *B* after τ=1.3 turns to be negative, while the velocity of Point *E* approximates to 0. All these behaviors indicate that the differences in the spreading factor of the upper and lower rims come from the effects of gravity.

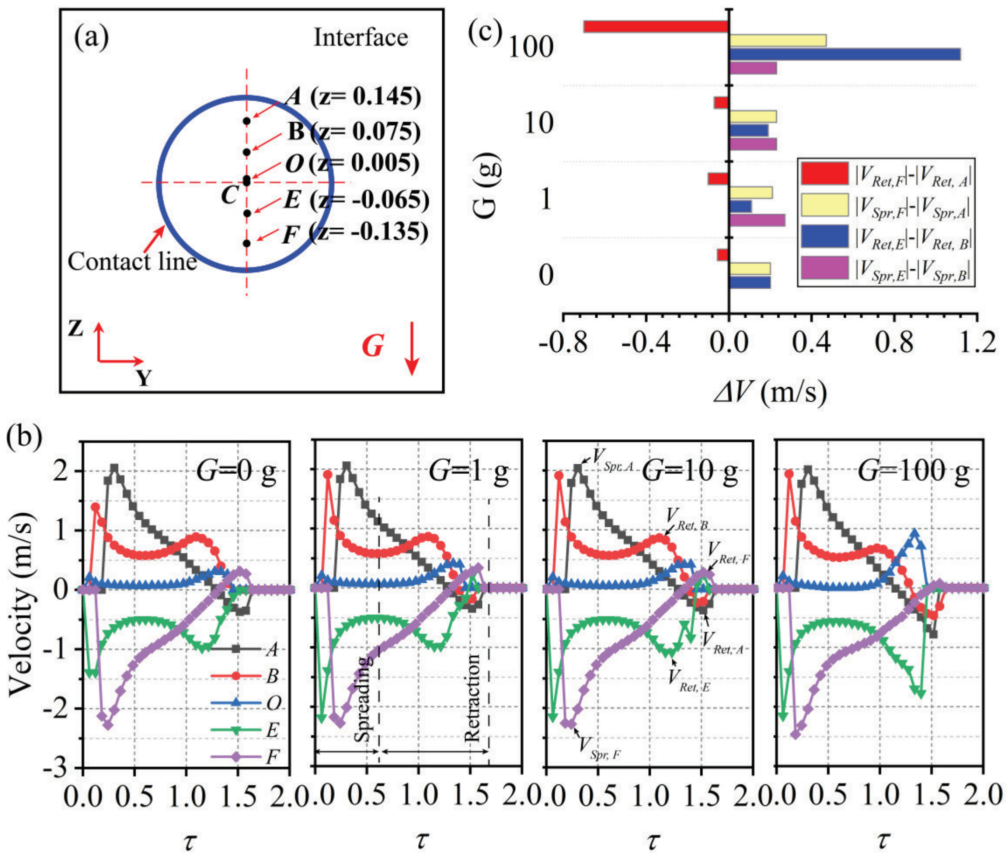

Fig. 7. (a) Coordinate of point A-F; (b) velocity evolution at five characteristic points under different gravity levels; (c) the differences in the velocity peak between E (F) and B (A).

Furthermore, Fig. 8 shows the spreading time, maximum spread time, and retraction duration of the first oscillation period of droplets in Case 1-Case 3. These characteristic times show an increment with the increase of substrate temperature, essentially exhibiting a dependence on solidification. Specifically, the spreading time of the upper rim is shorter than that of the lower one as the droplet spreads outward to its limits. The time required for the droplets to reach their maximum spread extent equals the spreading time of the lower rim, which means that the upper rim begins to retract at the moment that the lower rim reaches to its maximum extent. As the droplet retracts back inward, the retraction duration of the upper rim is also smaller than that of the lower rim for droplet in Case 1 and Case 2. As the droplet spreads out, the volume fraction of droplet spreads downhill is more than that spreads uphill because of gravity effects. In other word, the total heat of the downstream fluid is more than that of the upstream. Thus, the upper rim undergoes a fast solidification rate during spreading and retraction processes.

But the exception is that the retraction duration of droplet in Case 3 shows an completely opposite regular pattern compared to Case 1 and Case 2, that is the retraction duration of the upper rim is larger than the lower one. The reason is that there is no solidification occurs on the condition that substrate temperature is higher than the droplet melting point, resulting in that the upper rim of the droplet experiences acceleration by gravity during receding as the lower rim does in spreading. Consequently, the retraction extent of the upper rim is certainly larger than that of the lower one. This agrees well with the receding behaviors as shown in Fig. 6. Accordingly, it can be concluded that gravity is a nonnegligible effect on the differences in characteristic time for droplet spreading and receding.

Based on the above discussions, it shows that the velocity and characteristic time can indirectly embody the gravity effects on the asymmetrical spreading and retraction of the impacted droplet.

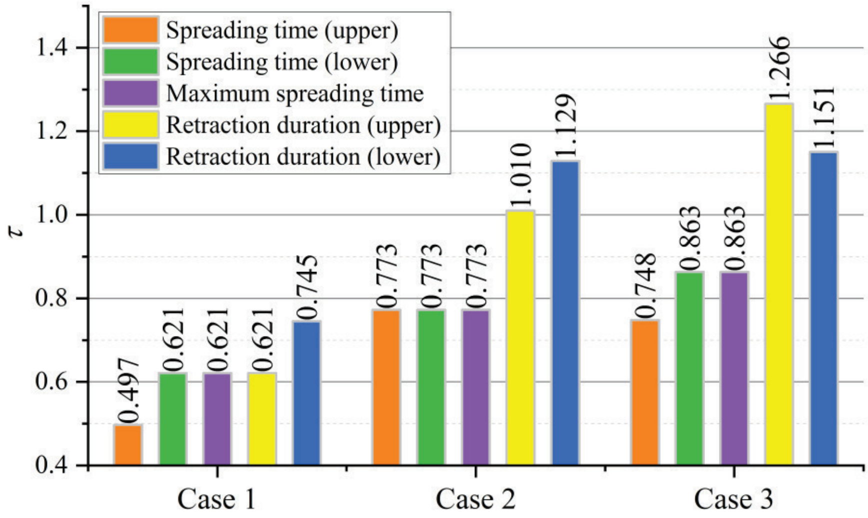

Fig. 8. Characteristic time for droplet spreading and receding in the first oscillation.

3.1.2. Mechanisms on the formation of asymmetrical solidification shape

It is found that the solidification shape of the droplet deposited on the vertical substrate is also asymmetric (the droplet tilts to gravity direction). To ascertain the formation of this undesired solidification shape, we investigated the variations of the vertex height D' (as seen in Fig. 1 (c)) and the tilt angle θ of the droplet versus the dimensionless time τ. As shown in Fig. 9 (a)-(b), the vertex D' oscillates with time until the droplet solidified. With higher substrate temperature, the oscillation decays slowly. Under the condition that the temperature of the substrate exceeds the melt point of the droplet (Fig. 9 (c)), the oscillation only decays by dissipation. During the droplet oscillating, θ varies synchronously with the vertex height. The peak values of θ present the instants when the vertex D' descends to the lowest position in every oscillation period. These values decrease with the decay of the oscillation. It indicates that the gravity effects behave more significantly when the droplet retracts back. The dynamic droplet inevitably shows an up-down oscillation after impacting on a vertical substrate.

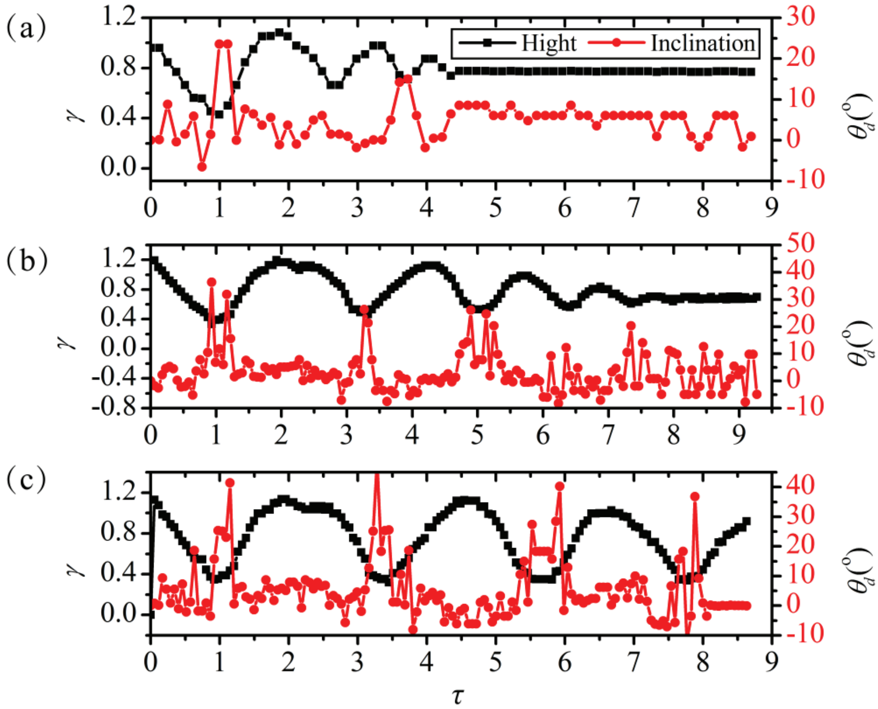

Fig. 9. The apparent dimensionless height and tilt angle of the droplet versus time in (a) Case 1; (b) Case 2; (c) Case 3.

To demonstrate the development of the tilt angle θ, the fluid field of the droplet in oscillation was investigated. Four different oscillation moments are shown in Fig. 10, Fig. 10 (a)-(b) are picked out from the first retraction period and Fig. 10 (c)-(d) from the second spreading period. Basically, the velocity field is asymmetric. Affected by gravity, the velocity vectors of the upper part are larger than the lower part when the droplet recedes inward. On the contrary, the vectors of the upper part are smaller than the lower part when the droplet spreads outward. As a result, the droplet oscillates up and down. Synchronously, the droplet solidifies from bottom to top. The up-down oscillation and solidification of the droplet interact with each other. Under the competition of oscillation and solidification, the solidifying phase propagates from bottom to top at the moment the droplet protuberates like a tower (Fig. 11 (b)), which is subject to a deflection induced by bending moment [36]. As a result, the solidified droplet behaves a noticeable tilt angle of θ. This undesired solidification shape would usually hinder a good fusion between neighboring droplets, resulting in that some hole-defects emerge. According to Yi and Qi et al. [37,38], the hole-defect comes from a time-dependent void region formed among two neighboring droplets and the substrate. It is because that under the drag effects from gravity, the residual liquid in the molten droplet trends to flow downwards. That is contrary to the direction of filling in the void region. To this end, the influence law and elimination strategy for the undesired solidification shape of droplets on vertical substrates should be studied, which will be discussed in the next section.

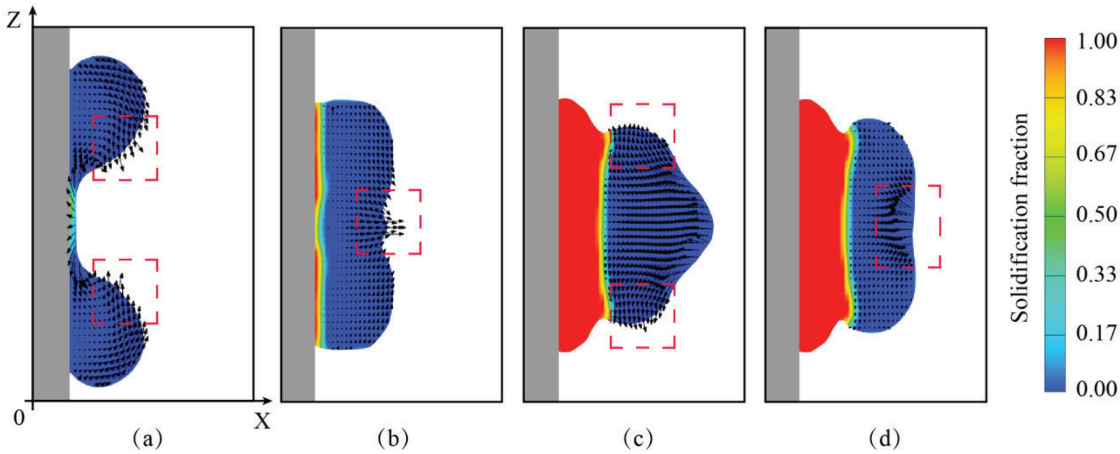

Fig. 10. Fluid field of the droplet in Case 1 at (a) 0.18 (τ=1.1), (b) 0.2 ms (τ=1.2), (c) 0.37 ms (τ=2.3), (d) 0.44 ms (τ=2.7).

To demonstrate the formation mechanisms of the aforementioned nonuniform fluid field that brings about the up-down oscillation, the forces (solidification drag, surface tension, and gravity) exerted on the droplet are analyzed as shown in Fig. 11. The droplet adhered on the vertical substrate can be regarded as a soft overhanging beam, which is subject to a bending moment [36] The droplet that protuberates like a tower as shown in Fig. 11 (b) tilts to gravity with a notable deflection during retraction, which presents as a downward oscillation. On contrast, as the outstretched droplet retracts back at spreading stage, it shows an upward oscillation (see Fig. 11 (a)). To further demonstrate this argument, the deflection equation is established. Fig. 11 (c) is an infinitesimal unit that captured from Fig. 11 (b) at *t* minute. There is

$$\rho A(x,t)\frac{\partial^2 w(x,t)}{\partial t^2} = -\frac{\partial Q(x,t)}{\partial x} \tag{5}$$

where ρ is density, $w(x, t)$ is the deflection of a point with an abscissa of x on the tower, $A(x, t)$ and $Q(x, t)$ are the area and shear force of the cross-section of the infinitesimal unit, respectively. The rotation equation of the infinitesimal unit is

$$Q(x,t) = \frac{\partial M(x,t)}{\partial x} \tag{6}$$

where $M(x, t)$ is the bending moment of the infinitesimal unit. Combining Eq. (5) and Eq. (6), there is

$$\rho A(x,t)\frac{\partial^2 w(x,t)}{\partial t^2} = -\frac{\partial^2 M(x,t)}{\partial x^2} \tag{7}$$

According to the mechanics of materials, there is

$$M(x,t) = EI(x,t)\frac{\partial^2 w(x,t)}{\partial x^2} \tag{8}$$

where $EI(x, t)$ denotes the bending rigidity of the cross-section. Substituting Eq. (8) into Eq. (7), we obtained

$$\rho A(x,t)\frac{\partial^2 w(x,t)}{\partial t^2} = -\frac{\partial^2}{\partial x^2}\left[EI(x,t)\frac{\partial^2 w(x,t)}{\partial x^2}\right] \tag{9}$$

Given a certain instant, the general solution of w can be expressed as

$$w_n = K_1\left[\left(\cosh\beta_n x - \cos\beta_n x\right)\right] + \frac{\cos\beta_n x_D + \cosh\beta_n x_D}{\sin\beta_n x_D + \sinh\beta_n x_D}\left(\sin\beta_n x + \sinh\beta_n x\right) \tag{10}$$

where K_1 is determined by the initial conditions of the velocity and displacement of the beam at t=0. x_D is the height of the droplet vertex. $\beta_n = \left(\rho A \omega^2{}_n / EI\right)^{1/4}$, ω_n are the natural frequencies of the dynamic droplet. Obviously, the deflection of the overhanging beam-like dynamic droplet follows vibration function. Accordingly, the droplet behaves an up-down oscillation.

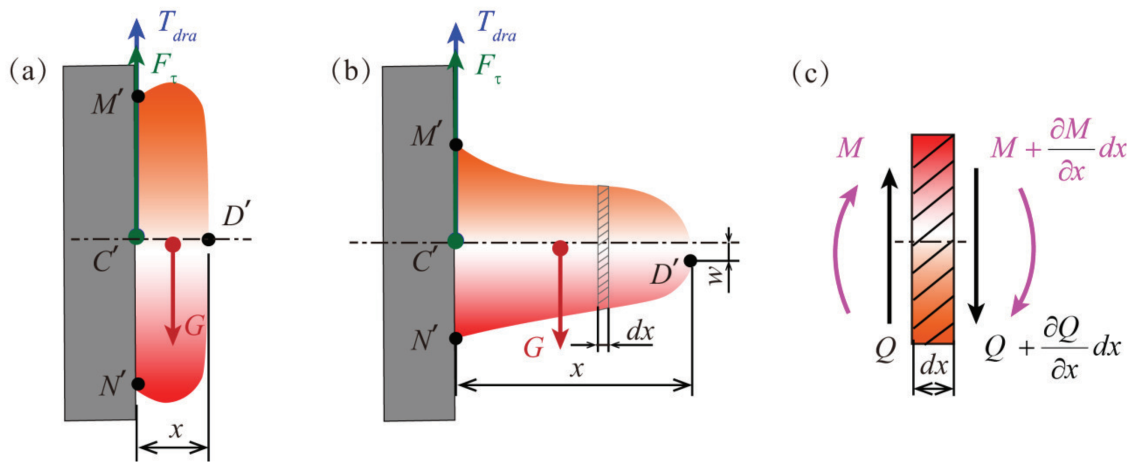

Fig. 11. Force schematics of droplet at (a) flat pancake shape (spreading) and (b) tower shape (retraction), (c) an infinitesimal unit captured from (b).

3.2 Effects on the undesired shape of the solidified droplets

3.2.1. Effects of impact velocity

To unravel the influence law on the undesired shape of the solidified droplets, the dependence of the tilt θ versus processing parameters were studied. As the *We* numbers of the droplets in Case 1-3 are approximately euqal to 13 and the Ohnesorge numbers (from here on *Oh*, which denotes the ratio of viscous forces to surface tension, $Oh = \mu / \sqrt{\rho \sigma d_0}$) do not exceed 0.01, the droplet spreading is mainly induced by the dynamic pressure gradient and resisted by inertia [39]. Therefore, the solidification shapes of droplets with impact velocities varying from 0.48 m/s to 1.63 m/s were investigated as shown in Fig. 12 (a)-(e). The initial temperatures of the droplet and substrate are ~250 ºC and ~140 ºC, respectively. As shown in Fig. 13, the tilt angle θ of the solidified droplet decreases with the increase of the *Fr* number. As illustrated in the previous section, when the rim of the droplet retracts back to its minimal diameter, the receded droplet is analogous to an overhanging beam, which is subject to a bending moment because of gravity. Since the spreading diameter of the droplet increases with the *Fr* number [40], the height of the top vertex is large under the condition of small *Fr* number. Accordingly, the droplet is correspondingly subject to a large bending deflection. Finally, the droplet solidifies into an obvious tilt shape (characterized as θ).

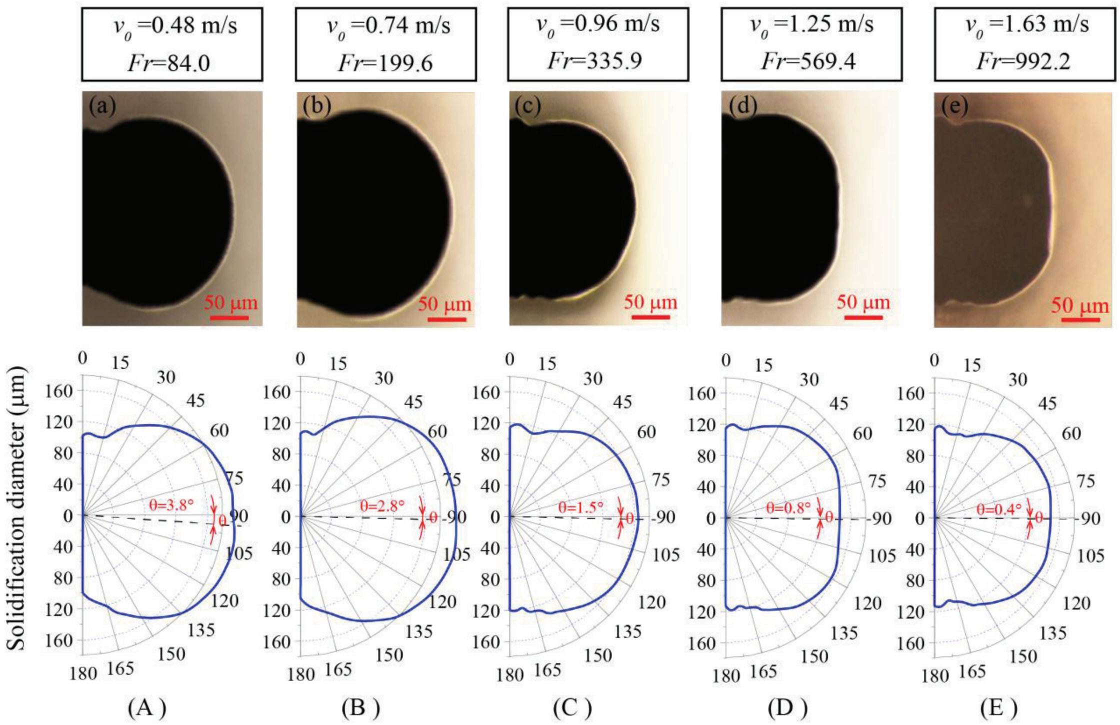

Fig. 12. Solidified droplets under various initial velocity: (a) - (e) micrographs, (A) - (E) contours of (a) - (e), respectively.

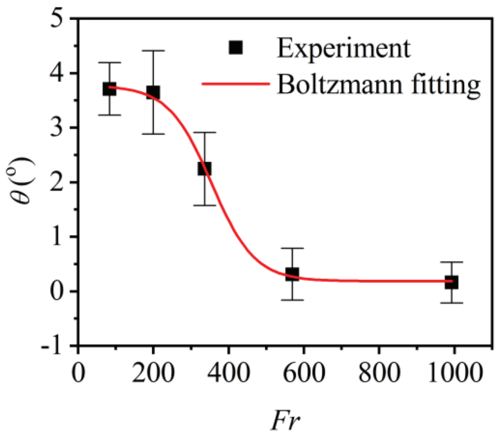

Fig. 13. Dependence of θ on the *Fr* number of droplets.

When the *Fr* number of the droplet is larger than 600, θ is less than 0.5°. This small tilt angle could be neglected in the printing process because there might exist an inherent asymmetry [35] of solidified droplets owing to the effects of ejection errors [10] and nonuniform wetting of the substrate surface.

3.2.2. Effects of droplet temperature

As a molten metal droplet deposits on the substrate, the heat of the droplet transfers to the substrate accompanied by fluid dynamics. The initial temperatures of the droplet and substrate have a crucial impact on the final solidification shape of the droplet. As shown in Fig. 14 (a)-(f), by varying the initial temperature of the droplet, different solidification shapes are observed. The dimentionless number superheat parameter (*SHP*) [33] is used to characterize the heat of the droplet. In Fig. 14, the substrate temperature is 140 ºC, and the impact velocity is 0.96 m/s. The dependence of θ on *SHP* is shown in Fig. 15. The value of θ increases with the increase of *SHP* firstly, but then decreases as the *SHP* of droplet is larger than 0.65. When *SHP* is smaller than 0.5 or larger than 0.8, θ is less than 0.5°. In this parameter interval, the deposited droplet could solidify into a good solidification shape. However, as shown in Fig. 14 (a) , the solidification angle is obviously large with small *SHP* (<0.5), which is not conducive to printing because of the drawback of easily forming hole-defects between two neighbouring droplets and substrate. Therefore, only the parameter interval *SHP* > 0.8 is appropriate for printing.

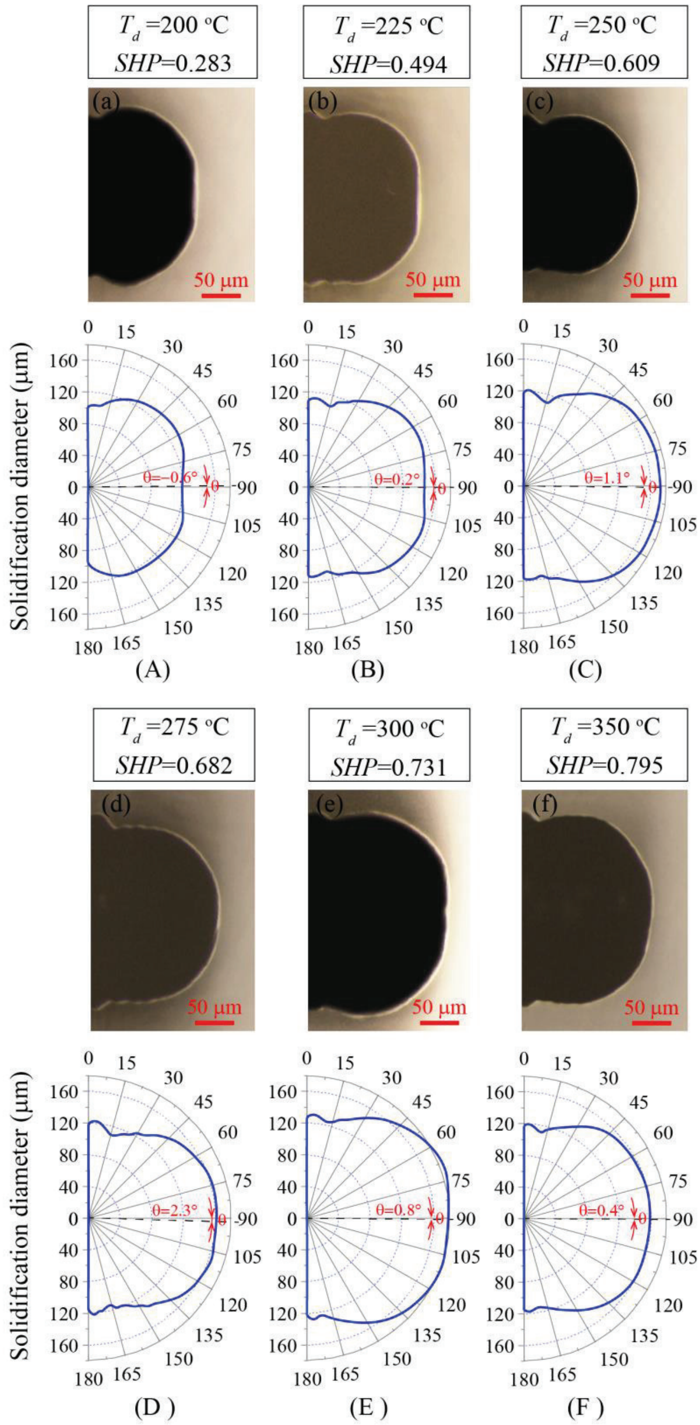

Fig. 14. Solidified droplets under various droplet temperature: (a) - (f) micrographs, (A) - (F) contours of (a) - (f), respectively.

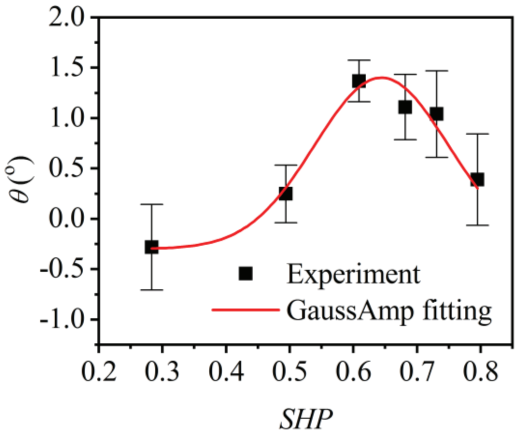

Fig. 15. Dependence of θ on the *SHP* number of droplets.

In Fig. 15, the variation of θ is attributed to the influence of droplet temperature on solidification time. According to Waldvogel et al. [33], the solidification time increases with droplet temperature. For a lower droplet temperature, the rim of the droplet solidifies before it retracts back due to the rapid solidification of the droplet bottom. Therefore the spread diameter is relatively large, and the height of the top vertex of the droplet is relatively small. Conversely, when the droplet temperature is high, the solidification rate is slow. The kinetic energy of the oscillating droplet reduces to a considerably low level before the rim of the droplet starts to solidify, resulting in low impact of the up-down oscillation of the droplet on solidification shape. For a moderate droplet temperature, the droplet starts to solidify during the retraction process. As a result, the undesired solidification shape shows up.

3.2.3. Effects of substrate temperature

In Fig. 16 (a)-(e), we introduced *Ste* number to characterize the thermal properties that pertains to substrates. The initial temperature of the droplet is 250 ºC, and the impact velocity is 1.63 m/s. The solidification shape of the droplet varies with different *Ste* number. As shown in Fig. 17, θ increases as the *Ste* number of the substrate increases from 0.3 to 0.4, and keeps constant when *Ste* is smaller than 0.3 or larger than 0.4. What is different from Fig. 15 is that the droplet solidifies into an obvious tilt shape when the substrate temperature is low. In this case, we could get a regular solidification shape as the *Ste* number is less than 0.057. Similarly, a higher substrate temperature enables the oscillating droplet have plenty of time to make the kinetic energy reduce to a considerably low level before the rim of the droplet starts to solidify. That suppresses the oscillation effects on solidification.

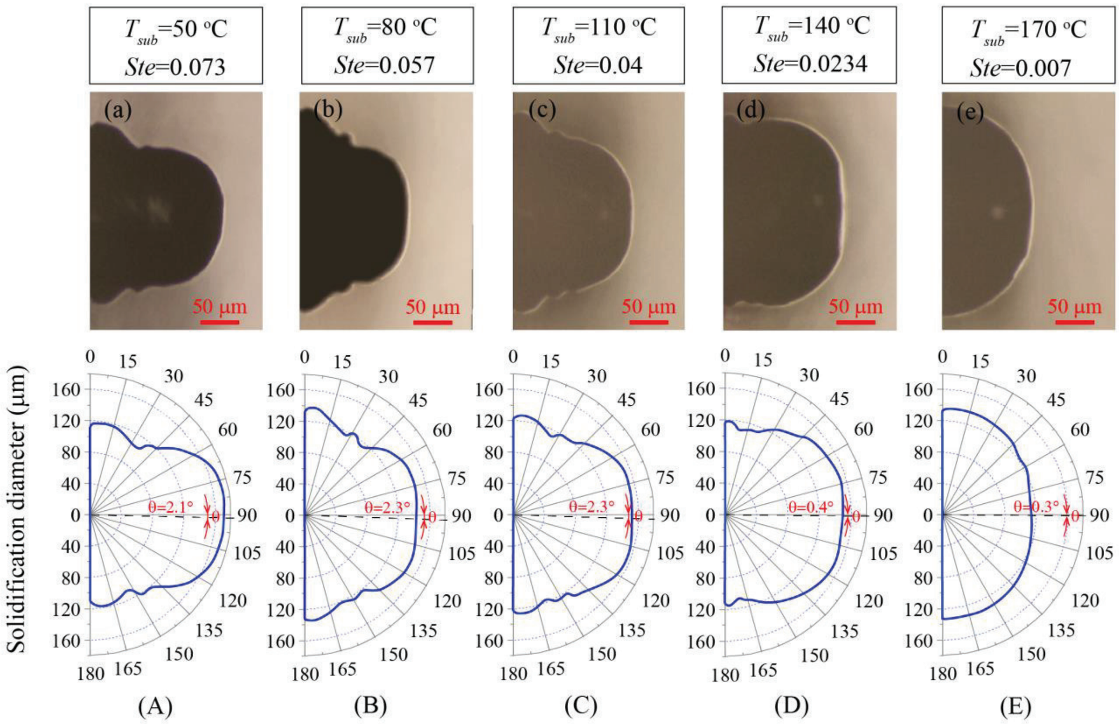

Fig. 16. Solidified droplets under various substrate temperature: (a) - (e) micrographs, (A) - (E) contours of (a) - (e), respectively.

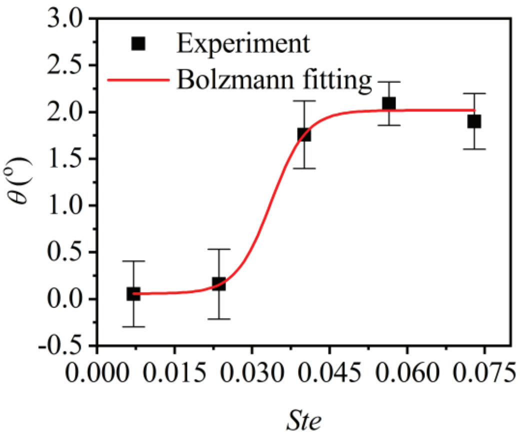

Fig. 17. Dependence of θ on the *Ste* number of droplet.

According to the investigation on the effects of impact velocity, temperatures of droplet and substrate, the undesired solidification shape of the deposited droplet on vertical substrates would be effectively eliminate by moderately improving the inertia and slowing the solidification rate of the droplet on the condition that no splash and over-remelting emerge. In future work, theoretical research should be developed to obtain a mapping between solidification shape and processing parameters. Moreover, the floating zone convection causing the difference of the microstructure in microgravity from that on the earth should also be eliminated by external field (i.e. surface acoustic waves (SAWs) [41], electric field [42], and magnetic fields [43]).

4. Conclusions

In summary, this work unveils the impact and solidification behaviors of molten metal droplets on vertical substrates through experiment and numerical simulation. As the droplet impacts on the substrate, tilt solidification shape arises due to the coupling effects of the asymmetrical spreading, up-down oscillation and solidification. The undesired solidification shape shows a dependence on the processing parameters such as impact velocity, the temperature of droplet and substrate, suggesting that the undesired solidification shape could be suppressed through appropriately selecting the processing parameters. With larger impact inertia or slower solidification rate, the undesired solidification shape would be effectively suppressed. This work provides a foundation to ground-based simulation of droplet deposition 3D printing under microgravity. Future works will be addressed to eliminate the gravity effect on the solidification shape and microstructure of the deposited droplet in ground-based simulation of printing processes through optimizing parameter combination and introducing external field.

Acknowledgements

This work was supported by the National Natural Science Foundation of China (No. 51675436, No. 51772245), and Aeronautical Science Foundation of China (2017ZE53057).

References

[1] J. Huang, L. Qi, J. Luo, L. Zhao, H. Yi, Suppression of gravity effects on metal droplet deposition manufacturing by an anti-gravity electric field, Int. J. Mach. Tools Manuf. 148 (2020) 103474.

[2] A. Hudson, 3D Printing in Space- Enabling New Markets and Accelerating the Growth of Orbital Infrastructure_Made In Space Inc, (2010) 14.

[3] M.J. Werkheiser, J. Dunn, M.P. Snyder, J. Edmunson, K. Cooper, M.M. Johnston, 3D Printing In Zero-G ISS Technology Demonstration, in: AIAA SPACE 2014 Conf. Expo., American Institute of Aeronautics and Astronautics, San Diego, CA, 2014.

[4] K. Cooper, C. McLemore, T. Anderson, Cases for Additive Manufacturing on the

International Space Station, in: 50th AIAA Aerosp. Sci. Meet. New Horiz. Forum Aerosp. Expo., American Institute of Aeronautics and Astronautics, Nashville, Tennessee, 2012.

[5] C.A. McLemore, B. Systems, E. Edmunson, IN SITU MANUFACTURING IS A NECESSARY PART OF ANY PLANETARY ARCHITECTURE. J., (2012) 2.

[6] R.A. Hafley, K.M.B. Taminger, R.K. Bird, Electron Beam Freeform Fabrication in the Space Environment, in: Electron Beam Free. Fabr. Space Environ., American Institute of Aeronautics and Astronautics, Reno, Nevada, 2007.

[7] A. Hudson, 3D Printing in Space- Enabling New Markets and Accelerating the Growth of Orbital Infrastructure_Made In Space Inc, in: Space Studies Institute, Mountain View, CA, 2010: pp. 1–14.

[8] K.G. Cooper, M.R. Griffin, Microgravity Manufacturing Via Fused Deposition, NASA Marshall Space Flight Center, Huntsville, AL, United States, 2003.

[9] D. Krantz, On-demand spares fabrication during space missions using Laser Direct Metal Deposition, in: AIP Conf. Proc., AIP, Albuquerque, New Mexico, 2001: pp. 170–175.

[10] Y. Chao, L. Qi, Y. Xiao, J. Luo, J. Zhou, Manufacturing of micro thin-walled metal parts by micro-droplet deposition, J. Mater. Process. Technol. 212 (2012) 484–491.

[11] L. Qi, S. Zhong, Three-dimensional printing technology based on uniform metal droplet ejecting, Sci. Sin. Informationis. 45 (2015) 212–223.

[12] K.R. Avchare, A. Tarwani, D. Jain, U. Saini, R. Purohit, Space manufacturing Techniques: A Review, 4 (2014) 10.

[13] F. Milinazzo, M. Shinbrot, A numerical study of a drop on a vertical wall, J. Colloid Interface Sci. 121 (1988) 254–264.

[14] P. Dimitrakopoulos, J.J.L. Higdon, On the gravitational displacement of three-dimensional fluid droplets from inclined solid surfaces, J. Fluid Mech. 395 (1999) 181–209.

[15] T. Podgorski, J.-M. Flesselles, L. Limat, Corners, Cusps, and Pearls in Running Drops, Phys. Rev. Lett. 87 (2001) 036102.

[16] S. Ravi Annapragada, J.Y. Murthy, S.V. Garimella, Droplet retention on an incline, Int. J. Heat Mass Transf. 55 (2012) 1457–1465.

[17] F. Milinazzo, M. Shinbrot, A numerical study of a drop on a vertical wall, J. Colloid Interface Sci. 121 (1988) 254–264.

[18] J. Xie, J. Xu, W. Shang, K. Zhang, Mode selection between sliding and rolling for droplet on inclined surface: Effect of surface wettability, Int. J. Heat Mass Transf. 122 (2018) 45–58.

[19] š. Šikalo, C. Tropea, E.N. Ganić, Impact of droplets onto inclined surfaces, J. Colloid Interface Sci. 286 (2005) 661–669.

[20] A. Al-Sharafi, B.S. Yilbas, H. Ali, N. AlAqeeli, A Water Droplet Pinning and Heat Transfer Characteristics on an Inclined Hydrophobic Surface, Sci. Rep. 8 (2018).

[21] Z. Jin, H. Zhang, Z. Yang, The impact and freezing processes of a water droplet on a cold surface with different inclined angles, Int. J. Heat Mass Transf. 103 (2016) 886–893.

[22] J.C. Bird, S.S.H. Tsai, H.A. Stone, Inclined to splash: triggering and inhibiting a

splash with tangential velocity, New J. Phys. 11 (2009) 063017.

[23] Y. Chao, L. Qi, H. Zuo, J. Luo, X. Hou, H. Li, Remelting and bonding of deposited aluminum alloy droplets under different droplet and substrate temperatures in metal droplet deposition manufacture, Int. J. Mach. Tools Manuf. 69 (2013) 38–47.

[24] D. Chatzikyriakou, S.P. Walker, G.F. Hewitt, C. Narayanan, D. Lakehal, Comparison of measured and modelled droplet–hot wall interactions, Appl. Therm. Eng. 29 (2009) 1398–1405.

[25] M. Romano, R. Guillaument, C. Hany, J.C. Batsale, C. Pradere, Thermal analysis of droplet flow: Numerical, analytical and experimental investigations, Appl. Therm. Eng. 90 (2015) 403–412.

[26] S. Vincent, C.L. Bot, F. Sarret, E. Meillot, J.-P. Caltagirone, L. Bianchi, Penalty and Eulerian–Lagrangian VOF methods for impact and solidification of metal droplets plasma spray process, Comput. Fluids. 113 (2015) 32–41.

[27] H. Yi, L. Qi, J. Luo, N. Li, Hole-defects in soluble core assisted aluminum droplet printing: Metallurgical mechanisms and elimination methods, Appl. Therm. Eng. 148 (2019) 1183–1193.

[28] H. Li, 3D numerical simulation of successive deposition of uniform molten Al droplets on a moving substrate and experimental validation, Comput. Mater. Sci. (2012) 11.

[29] G.-X. Wang, E.F. Matthys, Experimental determination of the interfacial heat transfer during cooling and solidification of molten metal droplets impacting on a metallic substrate: effect of roughness and superheat, Int. J. Heat Mass Transf. 45

(2002) 4967–4981.

[30] T. Loulou, E.A. Artyukhin, J.P. Bardon, Estimation of thermal contract resistance during the first stages of metal solidification process: II-experimental setup and results, Int. J. Heat Mass Transf. 42 (1999) 2129–2142.

[31] S.D. Aziz, S. Chandra, Impact, recoil and splashing of molten metal droplets, Int. J. Heat Mass Transf. 43 (2000) 2841–2857.

[32] X. Chao, L. Qi, W. Tian, Y. Lu, H. Li, Potential of porous pyrolytic carbon for producing zero thermal expansion coefficient composites: A multi-scale numerical evaluation, Compos. Struct. 235 (2020) 111819.

[33] J.M. Waldvogel, D. Poulikakos, Solidification phenomena in picoliter size solder droplet deposition on a composite substrate, Int. J. Heat Mass Transf. 40 (1997) 295–309.

[34] M. Pasandideh-Fard, R. Bhola, S. Chandra, J. Mostaghimi, Deposition of tin droplets on a steel plate: simulations and experiments, Int. J. Heat Mass Transf. 41 (1998) 2929–2945.

[35] W. Xiong, L. Qi, J. Luo, D. Zhang, J. Liang, H. Yi, Experimental investigation on the height deviation of bumps printed by solder jet technology, J. Mater. Process. Technol. 243 (2017) 291–298.

[36] S. Tang, Y. Bhimavarapu, S. Gulec, R. Das, J. Liu, T. Whitehead, C.-W. Yao, R. Tadmor, Droplets Sliding down a Vertical Surface under Increasing Horizontal Forces, (2019) 8.

[37] H. Yi, L. Qi, J. Luo, D. Zhang, H. Li, X. Hou, Effect of the surface morphology of

solidified droplet on remelting between neighboring aluminum droplets, Int. J. Mach. Tools Manuf. 130–131 (2018) 1–11.

[38] L. Qi, H. Yi, J. Luo, D. Zhang, H. Shen, Embedded printing trace planning for aluminum droplets depositing on dissolvable supports with varying section, Robot. Comput.-Integr. Manuf. 63 (2020) 101898.

[39] S. Schiaffino, A.A. Sonin, Molten droplet deposition and solidification at low Weber numbers, Phys. Fluids. 9 (1997) 3172–3187.

[40] L. Suli, W. Zhengying, D. Jun, W. Pei, L. Bingheng, A Numerical Analysis on the Metal Droplets Impacting and Spreading out on the Substrate, Rare Met. Mater. Eng. 46 (2017) 893–898.

[41] A. Rajapaksa, A. Qi, L.Y. Yeo, R. Coppel, J.R. Friend, Enabling practical surface acoustic wave nebulizer drug delivery via amplitude modulation, Lab. Chip. (2014) 8.

[42] S.-Y. Tang, V. Sivan, P. Petersen, W. Zhang, P.D. Morrison, K. Kalantar-zadeh, A. Mitchell, K. Khoshmanesh, Liquid Metal Actuator for Inducing Chaotic Advection, Adv. Funct. Mater. 24 (2014) 5851–5858.

[43] W.-Z. Fang, S. Ham, R. Qiao, W.-Q. Tao, Magnetic Actuation of Surface Walkers: The Effects of Confinement and Inertia, Langmuir. (2020) 26.